Classification of Neocortical Neurons Using Affinity Propagation

Naureen Ghani[1]*, Rafael Yuste[2]
[1]The Fu Foundation School of Engineering and Applied Science, Columbia University, New York, NY, USA; [2]Department of Biological Sciences, The Kavli Institute for Brain Science, Columbia University, New York, NY, USA

Abstract

Determining the circuitry of the neocortex requires an understanding of its components, which in turn necessitates a classification scheme of neocortical neurons. The neocortex consists primarily of excitatory pyramidal neurons (~80% of neocortical neurons) and inhibitory interneurons (~20% of neocortical neurons). Neocortical interneurons are ideally positioned to control circuit dynamics. GABAergic interneurons, in particular, largely contribute to the vast morphological and physiological variability of the cortex. However, much is still not known regarding these interneurons. Here we use unsupervised learning methods, such as PCA followed by k-means analysis, to create quantitative and unbiased classification schemes. We explored the use of affinity propagation, a novel exemplar-based method of cluster analysis, to quantitatively classify a diverse set of 337 neocortical interneurons. Each neuron was characterized by whole-cell recordings done by patch-clamping and complete 3D anatomical reconstructions. It was revealed that each interneuron subtype is characterized by a unique set of morphological and electrophysiological features that allowed for specialized function within the neocortical circuit. Affinity propagation may then be used to classify neurons, the first step to reverse engineer a neocortical circuit.

Introduction

Developmental neuroscience is an emerging field that harnesses powerful computational and mathematical techniques to model the brain. The goal of our research is to build a classification scheme of all neocortical neurons in a major effort to determine the circuitry of the neocortex.

The neocortex is the top layer of the cerebral hemispheres and is about 2 to 4 mm thick. It is composed of six layers, labeled I to VI (with I being the outermost layer and VI being the innermost layer). Along with the archicortex and paleocortex, the neocortex is one of three components of the cerebral cortex, accounting for 76% of the volume of the cerebral cortex. The neocortex is one of the most significant components of the brain and is involved in higher mental functions such as perception, memory, imagination, language, and music.

Since the neocortex participates in such a vast array of computational tasks, it is often compared to a parallel computer, which can carry out multiple calculations simultaneously. The underlying principle of parallel computing is that large problems can be divided into smaller ones, which are then solved concurrently or "in parallel." In other words, many computing elements are wired together and then operate in parallel. Furthermore, for every computing element added, it is often necessary to add new wires from the new addition to existing elements. Thus, the number of wires increases much more rapidly than the number of computers: 3 wires for 3 computers, 6 wires for 4 computers, 10 wires for 5 computers, and so on.

Extending this analogy to the brain, we would need a brain the size a football field to encompass billions of neurons (biological computing elements) that are all wired together. A real brain however selectively wires neurons together, omitting any unneeded wires (axons) for proper function. This simple mathematical analogy hints at many aspects of the brain. For instance, as mammals grow larger with evolution, the brain similarly increases in size, and the "cost" of wires grows severe. Neuroanatomical studies have quantitatively shown that the number of

 Received 1/1/2014. Accepted 3/14/2014. Published 3/14/14.
*To whom correspondence should be addressed: Naureen Ghani, Columbia University, New York NY 10027, email: ng2410@columbia.edu.

axons varies greatly region to region in the brain; some areas are heavily linked to others with massive axon tracts while others are far less strongly linked.

Many strides have been made in understanding the formation and function of neocortical circuits using detailed morphological and electrophysiological analyses of the neurons. Each of these model circuits differ greatly in form and content, however, because they each have different theoretical and experimental considerations. For historical reasons, many early neocortical circuit models are based on data from cat and primary visual cortex. In recent years, the rat somatosensory cortex has grown in prominence as a tool for understanding the cortex.

The idea of a canonical circuit has previously been applied to aspects of the vertebrate brain and spinal cord. It is highly relevant to questions of evolution, development, and homology of form and function. Supporting this idea is the close similarities in basic organization across vertebrate brains. Similarly, recognizable neuronal subtypes have been found across the neocortices of different mammalian species[15]. For these reasons, we hypothesize the existence of a canonical cortical microcircuit and it implements a relatively simple computation.

To create a neocortical circuit model, a classification scheme must first be established to outline the components of the cortex. In the past, cell type classification was qualitative and led to inconsistent subtypes. In recent years, the standard method for classification of neurons has been quantified through unsupervised cluster analysis[2, 4, 7, 8, 9, 11, 12]. Unsupervised cluster analysis is the classification of a set of data or objects into subsets (clusters) so that the data in each subset shares a common feature without any prior knowledge. One widely-used technique has been Ward's method with hierarchical clustering. Hierarchical agglomerative clustering is a bottom-up technique and begins by grouping the two "closest" cells as defined by the algorithm, and then continues to join the next "closest" cells and so forth. This method does not require specifying the number of clusters in advance and generates smaller clusters that may be helpful for discovery. However, one of the main disadvantages of hierarchical clustering is that once two cells are linked, they remain joined together in the final hierarchy. Moreover, hierarchical clustering is susceptible to a chaining effect in which objects may be "incorrectly" assigned to a cluster at an early stage instead of being grouped in new clusters.

Additional clustering techniques include k-means analysis k-metoids analysis, and affinity propagation. In k-means, each cluster is represented by the center of the cluster and in k-metoids analysis, each cluster is represented by one of the objects in the cluster. Affinity propagation is one of the most recently developed unsupervised clustering techniques. Each data point is viewed as a node in a network, and real-valued messages are transmitted between the data points until a set of exemplars and corresponding clusters is determined by the algorithm. Thus, at any point in time, the magnitude of each message reflects the current affinity that one data point has for choosing another data point as its exemplar, hence the name of "affinity propagation"[6].

In this work, we explore the application of affinity propagation to classification of neocortical neuronal subtypes. The algorithm was used to blindly classify a test dataset of four interneuron subtypes. The dataset included unlabeled cells in addition to known cells, the latter serving as a ground truth. The dataset is comprised of 67 morphological variables and 20 electrophysiological variables describing (1) parvalbumin-positive (PV+) basket cells (BC), (2) PV+ chandelier cells (ChC), (3) somatostatin-positive (SOM+) Martinotti cells (MC), and (4) SOM+ non-Martinotti cells (non-MC) as previously described in research[12]. We found that affinity propagation generates a fair classification in separating these four known interneuron subtypes and may be a powerful classification tool in discovering or defining neuronal cell types.

Materials and Methods

Preparation of Brain Slices

Acute brain slices were prepared from Nkx 2.1, G42, or GIN mice, with an average of 15 postnatal days (range P13 – P25). Mice were immediately decapitated, the brain was removed and then immediately placed in a cold sucrose cutting solution (222 mM sucrose, 2.6 mM KCl, 27 mM $NaHCO_3$, 1.5 mM NaH_2P_4, 0.5 mM $CaCl_2$, 3 mM $MgSO_4$, bubbled with 95% O_2, 5% CO_2). Coronal slices of 300 μm thickness were cut using a Vibratome and then transferred to a

holding chamber at room temperature with oxygenated ACSF (126 mM NaCl, 3 mM KCl, 3 mM $MgSO_4$, 1 mM CaCl2, 1.1 mM NaH_2PO_4, 26 mM $NaHCO_3$, and 10 mM dextrose, bubbled with 95% O_2, 5% CO_2). The slices were left to equilibrate with the room temperature for at least 30 minutes. Slices were then transferred to a recording chamber with the perfusion of ACSF bubbled with 95% O_2, 5% CO_2.

Transgenic Mouse Lines

To identify different types of interneurons, we used three transgenic mouse lines. First, we used the G42 line that labels PV+ cells[2]. PV+ cells are rapid spiking interneurons with basket or ChC morphology. We are able to identify basket cells from chandelier cells by their distinctive morphologies and threshold spiking responses. In addition, the chandelier cells have specially shaped axon arbors, in which axon terminals form distinct arrays called "cartridges" that we can visualize via GFP17. The Nkx2.1 line labels a population of interneurons that express the transcription factor Nkx 2.1, which includes interneurons that migrate from the medial ganglionic eminence (MGE), most notably ChCs17. A significant proportion of the ChC cells were found at the top of layer II, close to the layer I border, in both the G42 and Nkx 2.1 lines17. Finally, we used the GIN line to label SOM+ cells12. SOM+ cells are regular spiking interneurons with diverse morphology. In previous work, we determined three unique subtypes of SOM+ interneurons in GIN mice based on morphology and physiology: Martinotti cells and two novel subtypes12. As a result, we now distinguish between Martinotti cells (MC) and two novel subtypes (non-MC).

Electrophysiology Recordings

Brain slices were placed in a recording chamber at room temperature with a constant supply of oxygenated ACSF. Pipettes of 3-7 MΩ resistance were pulled from borosilicate glass. Whole cell recordings of cells were obtained using patch-clamping. Only cells with a healthy resting membrane potential (between -55 and -80 mV) were selected for recording.

Electrophysiological Analysis

20 variables were measured for each neuron by analysis of the recordings in MATLAB. The Petilla terminology scheme was used to name each variable describing firing and passive properties1. See Appendix 1 for descriptions.

Histological Procedure

Neurons were filled with biocytin by a patch pipette. Slices were kept overnight in 4% formaldehyde in 0.1M phosphate buffer (PB) at 4°C. Slices were then rinsed three times for five minutes per rinse on a shaker in 0.1M PB. They were then placed in 30% sucrose mixture (30g sucrose dissolved in 50 ml ddH_2) and 50 ml 0.24M PB per 100 ml) for 2 hours and then frozen on dry ice in tissue freezing medium. The slices were kept overnight in a -80°C freezer. After defrosting, the slices were rinses in 0.1M PBthree times, twenty minutes each, to remove tissue freezing medium. Slices were then incubated in 1% hydrogen peroxide in 0.1M PB for thirty minutes to pretreat the tissue. They were then rinsed twice in 0.02M potassium phosphate saline (KPBS) for twenty minutes. Afterwards, the slices were kept overnight in Avidin-Biotin-Peroxidase Complex. The slices were next rinsed three times in 0.02M KPBS ((0.7 mg/ml 3,3"-diaminobenzidine, 0.2 mg/ml urea hydrogen peroxide, 0.06M Tris buffer in 0.02M KPBS)) for 20 minutes each. Each slice was observed under a light microscope and then mounted onto a slide using crystal mount.

Three-Dimensional Neuron Reconstruction and Morphological Analysis

Three-dimensional reconstructions of successfully filled and properly stained neurons were done using Neurolucida software (MicroBrightField). The neurons were viewed with a 100x oil objective on an Olympus BX51 upright light microscope. Differential interference contrast (DIC) microscopy was employed to see otherwise invisible features of the sample. The neuron's processes were traced manually while the program recorded the coordinates of the tracing, thus creating a three-dimensional reconstruction. In addition to the neuron, the pia and white matter were drawn. The Neurolucida Explorer program was used to measure 67 morphological variables of the reconstruction describing somatic,

dendritic, and axonal properties. See Appendix 2 for descriptions.

Affinity Propagation

Affinity propagation is a clustering algorithm based on "passing messages" between data points6. It aims to combine the advantages of affinity-based clustering and model-based clustering. Affinity propagation is similar to k-metoid clustering in that both algorithms output "exemplars" that either serve as representative data or the centers of the clusters. Unlike k-metoid clustering, the exemplars are not chosen randomly in affinity propagation. Affinity propagation takes an input of real-valued similarities between data points, where the similarity *s(i,k)* indicates how appropriate a data point is to serve as an exemplar for data point *i*. Negative Euclidean distance is used to measure similarity to minimize squared error: for points *xi* and *xk*, $s(i,k) = -||xi - xk||2$. The key advantage of affinity propagation is that it does not require the number of clusters to be specified beforehand, unlike *k-means* cluster analysis. Instead, affinity propagation takes as input a real number *s(k,k)* for each data point *k*, such that data points with larger values of *s(k,k)* are more likely to be selected as exemplars.

There are two types of messages exchanged between data points. The first type called the "responsibility" *r(i,k), is* sent from data point *i* to candidate exemplar point *k,* and represents how well-suited point *k* is to serve as the exemplar for point *i,* compared to all other potential exemplars for point *i*. The second type, called the "availability" *a(i, k),* is sent from candidate exemplar point *k* to point *i*, and reflects the compiled evidence for how appropriate it would be for point *i* to choose point *k* as its exemplar, taking into account the support from other points that point *k* should be an exemplar. *r(i,k)* and *a(i, k)* can be viewed as log-probability ratios. Initially, the availabilities are initialized to zero: $a(i, k) = 0$. Then, the responsibilities are computed as:

$$r(i,k) \leftarrow s(i,k) - max'k_{k'|k'\neq k}\{a(i,k') + s(i,k')\}$$

Availabilities will eventually fall below zero as points are assigned to other exemplars. This will decrease the effective values of the input similarities, removing candidate exemplars from the competition.

Whereas the competition is data-driven for responsibilities and all the candidate exemplars compete for the ownership of a data point, the availability update gathers evidence from data points as to which candidate exemplar would make a good exemplar. The availability *a(i,k)* is set to the self-responsibility plus *r(k, k)* plus the sum of the positive responsibilities candidate exemplar *k* receives from other points:

$$a(i,k) \leftarrow \min\left\{0,\ r(k,k) + \sum_{i'\neq i,k} \max\{0, r(i',k)\}\right\}$$

Self-availability *a(k, k)* reflects evidence that *k* is an exemplar based on positive responsibilities sent to candidate exemplar *k* from other points:

$$a(k,k) \leftarrow \sum_{i'\neq k} \max\{0, r(i',k)\}$$

To evaluate the quality of a clustering produced by affinity propagation, we considered two aspects:

(1) the number of points that are correctly classified

(2) the number of clusters

With affinity propagation, we make the assumption that the identities of the exemplars are known, and so the number of correctly classified points may artificially increase. Therefore, we compute the classification accuracy as the ratio between correctly classified points (excluding the exemplars) and the total number of points (excluding the exemplars). In addition, a low number of clusters is preferred.

Results

Database of three known interneuron subtypes

We explored the use of affinity propagation to classify neocortical interneurons based on their morphological and physiological properties. In order to test the affinity propagation algorithm, we used a dataset where the identities of the neurons were known from previous studies12, 13, 17. More specifically, we used a physiology database that contained 337 interneurons distributed as: 57 somatostatin-positive cells (SOM+), 87 chandelier cells (ChC), and 193 parvalbumin-positive cells (PV+). The morphology database consisted of 111 interneurons distributed as: 24 ChC, 55 SOM+ and 32 PV+. Lastly, there were 51 neurons in a

database that consisted of both morphology and physiology variables, formed by an intersection of the two databases. Its distribution was: 12 PV+, 16 SOM+ and 23 ChC.

Affinity propagation classification of interneuron morphologies

The analysis of the morphology database resulted in 2 clusters (Figure 1). The first cluster consists of 84 neurons while the second cluster had 27 neurons. The first cluster had an exemplar of member 42, a SOM+ interneuron. It consists of: 22 ChC, 32 SOM+ and 30 PV+. Even though this cluster has an exemplar of SOM+ subtype, this cluster encompasses all the PV neurons with an accuracy of 93.75%. However, it only classifies 26.19% of the SOM+ interneurons correctly. The second cluster consists of: 2 CC, 23 SOM+ and 2 PV+. Its exemplar is member 83, a SOM+ neuron. Thus, 85.9% of the SOM+ neurons were correctly classified. This suggests that the second cluster with an exemplar of member 83 is truly representative of SOM+ neuronal subtype while the first cluster is representative of the PV subtype.

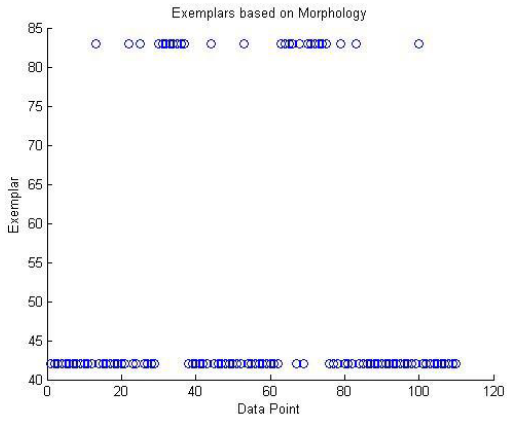

Figure 1: Using 20 electrophysiological variables, 110 interneurons were classified into 2 clusters by affinity propagation where the exemplars are members 42 and 83.

Affinity propagation classification of interneuron physiologies

The analysis of the physiology database revealed 3 distinct clusters (Figure 2). The first cluster consisted of 57 SOM+ neurons with an exemplar of member 21, also a member of the SOM+ subtype. Hence, 100% of the SOM+ neurons were correctly classified by the affinity propagation algorithm. The second cluster consisted of 8 PV+ and 87 CC neurons, where the exemplar was a part of the CC class (member 322). It correctly classified 90.80% of the CC neurons. The third cluster consisted of 142 CC and 51 PV+ and had an exemplar of 326, a member of the PV class. While the exemplar was representative of the PV+ subtype, only 26.42% of the PV+ neurons were correctly classified.

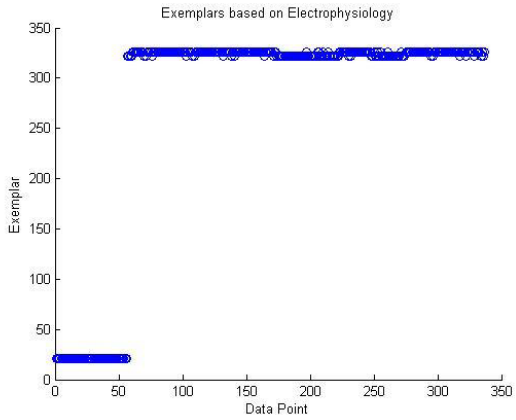

Figure 2: Using 67 electrophysiological variables, 337 interneurons were classified into 3 clusters by affinity propagation where the exemplars are members 21, 322, and 326.

Affinity propagation classification of interneuron joint databases

The analysis of the interneuron joint database resulted in 2 clusters (Figure 3). The first cluster consisted of: 6 PV, 8 SOM, and 17 CC. The exemplar was member 4, a member of the PV subtype. It correctly classified a mere 19.37% of PV neurons. The second cluster consisted of: 6 PV, 8 SOM, and 6 CC. The exemplar was member 38, a member of the CC subtype. Only 30% of the CC neurons were correctly classified.

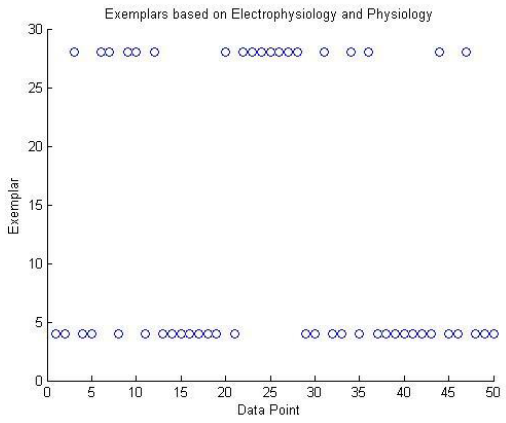

Figure 3: Using 67 morphological variables and 20 electrophysiological variables, 50 interneurons were classified into 2 clusters by affinity propagation where the exemplars are 4 and 48.

Discussion

Affinity propagation: An Exploratory Tool for Classification of Neural Data

In this study, we have explored the use of a new algorithm, affinity propagation, for the classification of neuronal data. We used a database of 337 neocortical GABAergic interneurons. Interneurons previously identified served as a ground truth, and acted as a measure for how accurate the algorithm was. The data was based on a collection of morphological and physiological data for each neuron. The classification accuracy we found was 0.56 for the Physiology database, 0.45 for the Morphology database, and 0.40 for the combined Morphology + Physiology database. The accuracy consistently decreased with a smaller data set, containing less information on neurons. The affinity propagation algorithm is able to consistently distinguish somatostatin neurons as a unique class among all three databases. However, difficulty arose s when the algorithm is asked to differentiate between chandelier cells and parvalbumin cells. In the Morphology database and the combined database, the cells were grouped into a single cluster consisting of large components of both chandelier cells and parvalbumin cells as opposed to two distinct clusters. After simplifying the database to include only chandelier cells and parvalbumin cells, while excluding somatostatin-positive cells, the affinity propagation algorithm is able to separate the cells into two clusters but with low accuracy (< 0. 50 for Physiology Database, the largest database was used).

The inability of the affinity propagation algorithm to separate chandelier cells and parvalbumin cells may be due to a number of potential reasons. One reason is that the chandelier cells and parvalbumin cells are morphologically and physiologically similar to one another. Recent research shows that chandelier neurons are a subset of GABA-ergic cortical interneurons that are said to be parvalbumin-containing and fast-spiking when innunostained16, thus distinguishing them from other GABAergic neurons, . Even though chandelier cells are truly distinct from other GABAergic neurons based on morphology with their unique axonal arbors, the affinity propagation algorithm correctly picks up this assumption.

Our observations may also be explained by potential sources of error. With a smaller dataset, the affinity propagation algorithm greatly decreased in accuracy. An additional error found in the dataset was that some of the measurements of input resistance were incorrectly normalized. The values less than 1 for resistance are reported in Giga Ohms while the values greater than 20 are reported in Mega Ohms.

Despite the moderate success of affinity propagation algorithm, we have insufficient evidence to reject it as an exploratory tool for neuronal classification. With a large enough dataset encompassing a much greater number of interneuron subtypes, we may be able to improved classification by affinity propagation. Such a dataset is in progress as we are manipulating the Windows Application Programming Interface (API) in an effort to automate the extraction of morphological data from Neuroexplorer. We have automated the clicks necessary to obtain the data of 67 morphological variables from a single neuron but we would like to implement this for the entire extraction process. Our goal is to create a dataset encompassing an estimated 1000 neurons of diverse interneuron subtypes, each characterized by an anatomical 3D reconstruction and whole-cell patch-clamp recording.

One great issue with classification schemes of neocortical neurons is that many markers, often transcription factors, exist to label

interneuron subtypes while there are few known markers to label pyramidal neurons. Moreover, pyramidal neurons account for a much larger percentage of the neocortex compared to interneurons (~ 4x as much). In the future, we would like to create an algorithm that separates pyramidal neurons from interneurons and will continue to research ways to classify pyramidal neurons. Affinity propagation and additional machine learning techniques have the potential to serve as powerful exploratory tools to build such classification schemes.

References

1. Ascoli, G.A.; Alonso-Nanclares, L.; Anderson, S.A.; Barrionuevo, G.; Benavides-Piccione, R.; Burkhalter, A.; *et al.* (2008). Petilla terminology: nomenclature of features of GABAergic interneurons of the cerebral cortex. *Nat. Rev. Neurosci.* 9, 557–568.
2. Cauli, B.; Audinat, E.; Lambolez, B.; Angulo, M.C.; Ropert, N.; Tsuzuki, K.; *et al.* (1997). Molecular and physiological diversity of cortical nonpyramidal cells. *J. Neurosci.* 17, 3894–3906.
3. Chattopadhyaya, B., Di Cristo, G., Wu, C.Z.; Knott, G.; Kuhlman, S.; Fu, Y.; *et al.* (2007). GAD67-mediated GABA synthesis and signaling regulate inhibitory synaptic innervation in the visual cortex. *Neuron* 54, 889–903.
4. DeFelipe, J. ; López-Cruz, P.; Benavides-Piccione, R.; Bielza, C.; Larrañaga, P.; Anderson, S.; *et al.* (2013). New insights in the classification and nomenclature of cortical GABAergic interneurons. *Nat. Rev. Neurosci.* 14, 202–216.
5. Douglas, R.J. and Martin, K.C. (2004). Neuronal Circuits of the Neocortex. *Annual Reviews of Neuroscience* 27, 419-451.
6. Frey, B.J. and Dueck, D. (2007). Clustering by passing messages between data points. *Science* 315, 972–976.
7. Helmstaedter, M.; Sakmann, B.; and Feldmeyer, D. (2009). L2/3 Interneuron groups defined by multiparameter analysis of axonal projection, dendritic geometry, and electrical excitability. *Cereb. Cortex* 19, 951–962.
8. Karagiannis, A.; Gallopin, T.; David, C.; Battaglia, D.; Geoffroy, H.; Rossier, J.; *et al.* (2009). Classification of NPYexpressing neocortical interneurons. *J. Neurosci.* 29, 3642–3659.
9. Karube, F.; Kubota, Y.; and Kawaguchi, Y.; (2004). Axon branching and synaptic bouton phenotypes in GABAergic nonpyramidal cell subtypes. *J. Neurosci.* 24, 2853–2865.
10. Liu, J.H.; Hansen, D.V.; Kriegstein, A.R.; Development and Evolution of the Human Neocortex. *Cell.* 2011 July 8. 146(I): 18-36.
11. Ma, Y., Hu, H., Berrebi, A.S., Mathers, P.H., and Agmon, A. (2006). Distinct subtypes of somatostatin-containing neocortical interneurons revealed in transgenic mice. *J. Neurosci.* 26, 5069–5082.
12. McGarry, L.M.; Packer, A.M.; Fino, E.; Nikolenko, V.; Sippy, T.; and Yuste, R. (2010). Quantitative classification of somatostatin-positive neocortical interneurons identifies three interneuron subtypes. *Front. Neural Circuits* 4:12.
13. Packer, A.M.; and Yuste, R. (2011). Dense, unspecific connectivity of neocortical parvalbumin-positive interneurons: a canonical microcircuit for inhibition. *J. Neurosci.* 31, 13260–13271.
14. Oliva, A.A. Jr.; Jiang, M.; Lam, T. ; Smith, K.L., ; and Swann, J.W.; (2000). Novel hippocampal interneuronal subtypes identified using transgenic mice that express green fluorescent protein in GABAergic interneurons. *J. Neurosci.* 20, 3354–3368.
15. Ramón y Cajal, S. (1911). *Histologie du Systeme Nerveux de l'Homme et des Vertebres.* Vol. 2. Paris: Maloine.
16. Taniguchi H.; Lu J.; Huang Z.J.; (2013). "The Spatial and Temporal Origin of Chandelier Cells in Mouse Neocortex". *Science* 339 (6115).
17. Woodruff, A.; Xu, Q.; Anderson, S. A.; and Yuste, R. (2009). Depolarizing effect of neocortical chandelier neurons. *Front. Neural Circuits* 3:15.

Appendices

Appendix 1: Electrophysiological Variables. Action potential properties measured from response to twice threshold, 500-ms current injection from first action potential (AP1) and second action potential (AP2). AP2 variables not listed as the same measurements were made for AP2 as listed for AP1.

Variable	Description
Rheobase (pA)	Threshold current
Resting membrane potential (mV)	Stable membrane potential when no c applied
AP1 amplitude (mV)	Amplitude of the 1st action potential (A
AP1 duration (ms)	Time from onset of 1st AP, calculated increase > 1 mV/100 ms, to offset, cal as return to same voltage as before A
AP1 half-width (ms)	Time from half-amplitude during rise t amplitude during fall of 1st AP
AP1 rise time (ms)	Time from onset to peak of 1st AP
AP1 fall time (ms)	Time from peak to offset of 1st AP
AP1 rise rate (mV/ms)	AP1 amplitude/ AP1 rise time
AP1 fall rate (mV/ms)	AP1 amplitude/ AP1 fall time
AP drop (mV)	AP1 amplitude – AP2 amplitude
Spike frequency adaptation	t_2/t_1, where t_1 is the time between the the first two APs (interspike interval) a the last interspike interval
Index of Accommodation	Average of the difference in length of consecutive interspike intervals norma the summed duration of these two inte intervals

Appendix 2: Morphological Variables. Variables were extracted using the Neurolucida Explorer Program by MicroBrightField.

Variable	Description
VARIABLES DESCRIBING THE SOMA	
Somatic Perimeter (μm)	Perimeter of the soma
Somatic Area (μm^2)	Area of the soma
Somatic Aspect Ratio	Max diameter of soma/ min diameter of soma
Somatic Compactness	((4/π)*Area)$^{1/2}$/ max diameter
Somatic form factor	(4π*Area)/(Perimeter^2)
Somatic Roundness	(4*Area)/(π* max diameter^2)
VARIABLES DESCRIBING THE AXON	
Axonal node total	Total number of axonal nodes (branching points)
Total axonal length (μm)	Sum of lengths of all axon segments, measured along tracing (not straight line distance)
Total surface area of axon (μm^2)	2πr2 + 2πrh, SA calculated by modeling axon as a cylinder with diameter of defined thickness in reconstruction
Ratio of axonal length to surface area (1/μm)	Total axonal length/ total surface area of axon
Highest order axon segment	Maximum number obtained after each segment is numbered by how many nodes it is removed from the initial segment
Axonal torsion ratio	Total axonal length/ total axonal length of fan in diagram where the fan in diagram is 2-D projection of the neuron constructed by compiling traces swept around a vertical axis. Torsion ratio = 1 corresponds to no loss of length, values larger than 1 correspond to factor by which the processes have decreased in the fan in diagram
K-dim of axon	Fractal dimension of axon calculated using linear regression and the nested cubes method
Axonal polar angle average	Average of polar angles of all axonal nodes. The polar angle is the angle between the 2 lines passing through the node and the endpoints of the next segments
Axonal polar angle standard deviation	Standard deviation of the axonal polar angles
Axonal local angle average	Average of local angles of all axonal nodes. The local angle is the angle between the 2 lines passing through the node and points adjacent to the node on the two following segments
Axonal local standard deviation	Standard deviation of axonal local angles
Axonal spline angle average	Average of spline angles of all axonal nodes. The spline angle is the angle between the 2 lines passing through the node and smoothed points adjacent to the node when the following two segments are approximated by a cubic spine
Axonal spline angle standard deviation	Standard deviation of axonal spline angles
Average tortuosity of axonal segments	Average of tortuosities measured for each axonal segment. Segment tortuosity = distance along segment/ straight line distance between the segment endpoints
Standard deviation of tortuosity of axonal segments	Standard deviation of tortuosities of all segments
Axonal segment length average (μm)	Total axonal length/ number of segments
Axonal segment length standard deviation (μm)	Standard deviation of axonal segment length
Average tortuosity of axonal nodes	Average of tortuosities measured for each axonal node. Node tortuosity = distance along process from origin of process to node/ straight line distance from origin of process to node
Standard deviation of tortuosity of axonal nodes	Standard deviation of tortuosities of all axonal nodes
Number of axonal sholl sections	Number of sholl sections (concentric spheres centered at the soma with radii at 100 μm intervals) containing axonal processes
Axonal sholl length at 100 μm	Total length of axonal segments contained in the first sholl section/ total axonal length
Axonal sholl length at 200 μm	Total length of axonal segments contained in the second sholl section/ total axonal length
Axonal sholl length at 300	Total length of axonal segments contained in the third sholl section/ total axonal length
Axonal sholl length density (μm)	Total axonal length/ number of axonal sholl sections
Axonal sholl node density	Axonal node total/ number of axonal sholl sections
Convex hull axon area (μm^2)	Area of the 2-D convex polygon created by connecting the distal axon segment endpoints of 2-D projection of neuron
Convex hull axon perimeter (μm)	Perimeter of the 2-D convex polygon created by connecting the distal axon segment endpoints of 2-D projection of neuron
Convex hull axon volume (μm^3)	Volume of the 3-D convex polygon created by connecting the distal axon segment endpoints
Convex hull axon surface area (μm^2)	Surface area of the 3-D convex polygon created by connecting the distal axon segment endpoints
Axon node density (1/μm)	Axonal node total/ total axonal length
VARIABLES DESCRIBING THE DENDRITES	
Number of dendrites	Total number of dendrites
Dendritic node total	Total number of dendritic nodes (branching points)
Total dendritic length (μm)	Sum of lengths of all dendrite segments, measured along tracing (not straight line distance)
Average length of dendrites (μm)	Total dendritic length/ number of dendrites
Total surface area of dendrites (μm^2)	See total surface area of axons
Ratio of dendritic length to surface area (1/μm)	See ratio of axonal length to surface area
Highest order dendrite segment	See highest order axonal segment
Dendritic torsion ratio	See axonal torsion ratio
K-dim dendrites	See K-dim axon
Dendritic polar angle average	See axonal polar angle average
Dendritic local angle standard deviation	See axonal local angle standard deviation
Dendritic spline angle average	See axonal spline angle average
Dendritic spline angle standard deviation	See axonal spline angle standard deviation
Average tortuosity of dendritic segments	See average tortuosity of axonal segments
Standard deviation of tortuosity of dendritic segments	See standard deviation of tortuosity of axonal segments
Dendritic segment length average (μm)	See axonal segment length average
Dendritic segment length standard deviation (μm)	See axonal segment length standard deviation
Average tortuosity of dendritic nodes	See average tortuosity of axonal nodes
Standard deviation of tortuosity of dendritic nodes	See standard deviation of tortuosity of axonal nodes
Number of dendritic sholl sections	Number of sholl sections (concentric spheres centered at soma with radii at 50 μm intervals) containing dendritic processes
Dendritic sholl length at 50 μm	Total length of dendritic segments contained in first sholl section/ total dendritic length
Dendritic sholl length at 100 μm	Total length of dendritic segments contained in second sholl section/ total dendritic length
Dendritic sholl length at 150 μm	Total length of dendritic segments contained in third sholl section/ total dendritic length
Convex hull dendrite area (μm^2)	See convex hull axon area
Convex hull dendrite perimeter (μm)	See convex hull axon perimeter
Convex hull dendrite volume (μm^3)	See convex hull axon volume
Convex hull dendrite surface area (μm^2)	See convex hull axon surface area
Dendrite node density (1/μm)	See axon node density
VARIABLES DESCRIBING LOCATION	
Relative distance	Distance from soma centroid to pia/ distance between pia and white matter

Appendix 3: Using 20 electrophysiological variables, 337 interneurons were visualized by creating the scatter plot matrix above of the two principal components of the neuronal data.

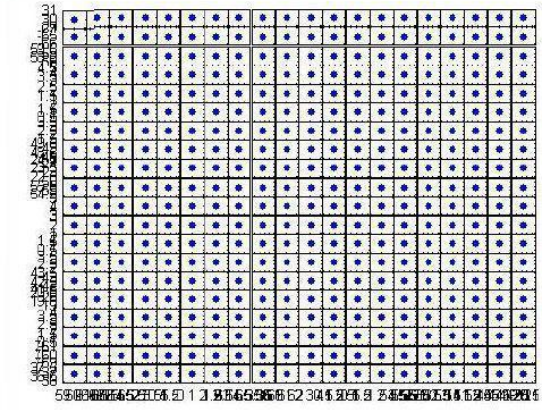

Appendix 4: Using 20 electrophysiological variables, a color map was made of 337 interneurons and hierarchical clustering was done, revealing 3 distinct clusters as did affinity propagation.